Ring Versus Bus: A Theoretical and Experimental Comparison of Photonic Integrated NoC

Paolo Pintus, *Member, IEEE*, Fabrizio Gambini, *Student Member, IEEE*, Stefano Faralli, Fabrizio Di Pasquale, Isabella Cerutti, and Nicola Andriolli

***Abstract*—Silicon photonics enables the fabrication of photonic integrated circuits with high bandwidth density, making it suitable for computercom applications. In multicore computing systems, the communications between cores and memory can be supported by optical networks-on-chip (NoC) realized with photonic integrated circuits (PIC). While different optical NoC topologies have been proposed in the past, only few NoC were fabricated and tested. This paper aims at comparing the performance of two PIC NoC with a bus and a ring topology. First, a framework is presented for passing from the theoretical analysis of silicon photonics basic building blocks like waveguides and microrings, to the PIC design and to the NoC performance derivation, using the scattering matrix method. Based on this framework, the two NoC topologies are simulated, designed, fabricated in silicon photonics, and experimentally characterized for comparison. Spectral performance validates the theoretical model with minor deviations due to the fabrication inaccuracies and limitations. Bit error rate performance at 10 Gb/s demonstrates the capability of simultaneous transmissions in both topologies with limited or negligible crosstalk. Moreover, ring NoC is shown to slightly outperform the bus NoC thanks to the filtering properties of the central microring.**

***Index Terms*—Integrated optics, optical network-on-chip, optical switches.**

I. Introduction

PHOTONIC integrated Circuits (PIC) provide a key technology for applications demanding communications at high bandwidth (BW) and throughput with a low power consumption. An excellent example of such applications is the computercom field that requires faster and faster transfer of data between cores and memories in the so-called *networks-on-chip* (NoC). Indeed, PIC solutions can offer the BW density and the latency uniformity [1]–[3] required for overcoming the limitations of electronic NoC (e.g., power density, synchronization issues, electromagnetic interference), thus enabling the continual scalability of computing systems [4], [5] according to Moore's law.

However, to fully exploit the PIC potentials, a well-assessed framework is required for passing from theoretical to experimental demonstration as developed through the years in the context of electronic circuits. Thus, the first challenge is the identification of a suitable framework for passing from the architectural design to PIC design, fabrication and characterization, ensuring the required specifications with adequate fabrication tolerance. In particular, the possibility of deriving a NoC-level model that abstracts the functionalities of the PIC without entering into technological details is of paramount importance for accelerating the simulations. An example is given by the libraries and tools for simulations of PIC NoC proposed in [6] and [7]. With a fast simulation tool of the NoC, it is possible not only to quickly predict the physical-layer performance and validate the measurements of the NoC but also to optimize the PIC design by assessing the sensitivity to the design parameters.

In addition, when exploiting photonic integrated devices, the second challenge is the identification of NoC architectures that can achieve the expected performance of high throughput, low delay variance, and low power consumption. Various NoC topologies have been realized with PIC: bus [8], [9], ring [10], space switches [11]–[13], Clos [14], crossbar [14]–[18] and characterized in terms of spectral performance [11]–[13] or bit error rate (BER) [11], [12]. Comparison between the various topologies has so far been carried out mainly at the theoretical level [14], [17].

This paper tackles these two fundamental challenges by considering two traditional NoC architectures, i.e., bus and ring, and by providing a thorough framework that goes from the mathematical modeling, to the PIC design, to the final characterization of the fabricated PIC. NoCs with ring and bus topology are selected as they can flexibly support multiple concurrent transmissions at low loss and without waveguide crossings. Bus is the widely used and studied topology due to its simplicity. Transmissions in both directions are possible by using two counter-propagating buses. Ring topology is typically preferred for the possibility to offer all-to-all communication even when unidirectional. However, the undesired recirculation may affect the signal quality. To achieve high energy efficiency, the PIC of the bus and ring NoCs are designed with solely passive photonic elements, i.e., waveguides and microrings. To model the physical layer of the microring-based NoCs and optimize the PIC design, an accurate theoretical framework is derived using the transfer matrix method based on a single microring add-drop block. PIC fabrication has been realized with silicon technology, which permits compatibility with electronics.

Manuscript received July 3, 2015; revised September 5, 2015 and September 24, 2015; accepted October 5, 2015. Date of publication October 11, 2015; date of current version November 1, 2015. This work was supported in part by the Italian Ministry of Education, University and Research through the FIRB project "MINOS," by the Italian Ministry of Foreign Affairs (MAE-UST) through the high-relevance bilateral project "NANO-RODIN," and by the European Commission through the FP7 project IRIS (619194).

P. Pintus and F. Gambini are with Scuola Superiore Sant'Anna, Pisa 56124, Italy, and also with the CNIT Photonic Networks National Laboratory, Pisa 56124, Italy (e-mail: paolo.pintus@sssup.it; fabrizio.gambini@cnit.it).

S. Faralli, F. Di Pasquale, I. Cerutti, and N. Andriolli are with Scuola Superiore Sant'Anna, Pisa 56124, Italy (e-mail: sfaralli@sssup.it; f.dipasquale@sssup.it; i.cerutti@sssup.it; n.andriolli@sssup.it).

Color versions of one or more of the figures in this paper are available online at http://ieeexplore.ieee.org.

Digital Object Identifier 10.1109/JLT.2015.2489698

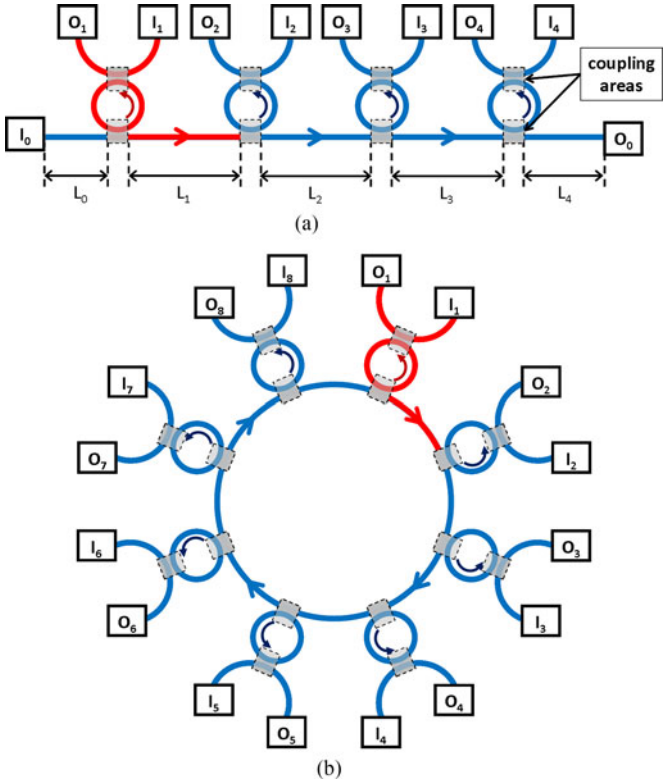

Fig. 1. Photonic integrated NoC architecture. The basic building block of the NoC is highlighted in the two figures. (a) Bus architecture. (b) Ring architecture.

The final objective of the work is to validate the framework by comparing the experimental and simulated performance of the fabricated PICs, and to gain further knowledge on the best performing microring-based NoC architecture(s). For this purpose, the simulation and experimental results of the physical-layer performance (i.e., spectra) are compared for both PICs. Moreover the data transmission performance (i.e., BER) of the bus NoC is compared with that of the ring NoC. Both comparisons are carried out considering the worst case scenario from the performance point of view, occurring when concurrent transmissions take place at the same wavelength leading to *homo-wavelength crosstalk* (XT)[19]–[21]. The results extend the initial works in [22] and [23] focusing on a single topology (i.e., ring), and in [24] limited to an experimental comparison, enabling the validation of the theoretical framework. The theoretical results provide also insights on the best NoC topology and the experimental results confirm that PIC technology is a viable solution for supporting concurrent transmissions on the same wavelength.

II. Photonic Integrated NoC Architectures

The bus and ring NoCs enable the communication between multiple tiles on a single chip (e.g., CPUs or shared memories). The integrated NoCs are realized with waveguides and microrings, as schematically shown in Fig. 1(a) and (b) for the bus and ring architecture, respectively. The communication between tiles occurs using optical signals, generated by laser sources, modulated by modulators and received by photoreceivers (not shown in the figure). Each modulated optical signal is injected in a shared waveguide (i.e., bus or ring) using the add port of a microring (i.e., input port I_i for $i = 1, \ldots, n$) and is then received from the desired drop port of the downstream microring (i.e., output port O_j for $j = 1, \ldots, n$). In addition, in the bus topology, the signal can also be injected directly into the bus at input port I_0 and extracted from the bus at output port O_0, as shown in Fig. 1(a).

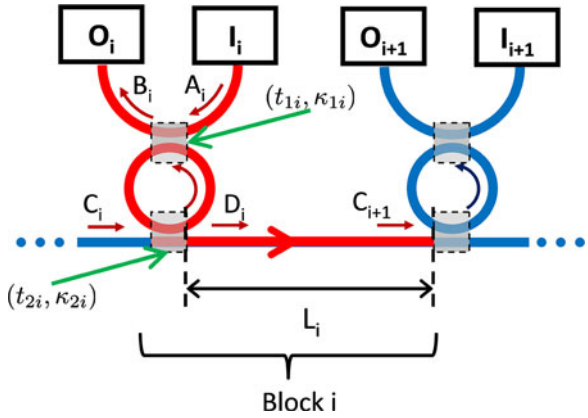

Fig. 2. Microring-based add/drop block.

Each microring acts either as an add or drop filter. Add and drop operations occur by properly tuning the microrings at the source and destination ports, enabling the communication between the ports as scheduled [25]. The wavelength of the added (or dropped) signals is fixed by the resonance wavelength of the microrings. The resonance of the local microring can be tuned by modulating the optical refractive index of the material, e.g., by exploiting thermal effects [26]. Once the microring is tuned, port I_i (O_i) is used for sending (receiving) the optical signal, while port O_i (I_i) (called dummy port) can be used for testing purposes (e.g., for controlling the resonance wavelength shift of the ring).

Next, the behavior of the bus and ring NoC is mathematically modeled.

III. Mathematical Model

Physical performance of the NoCs is modelled in terms of scattering coefficients using the transfer matrix method. For this purpose, the transfer matrix is derived first for a generic add/drop microring block as shown in Fig. 2.

In the figure, A_i and C_i are the input signals (i.e., the electric fields), while B_i and D_i are the output signals of the ith block. The relation between the input and output signals can be written as a function of the scattering matrix $\boldsymbol{Q}^{(i)}$ for the add/drop microring resonator [27]

$$\begin{pmatrix} B_i \\ D_i \end{pmatrix} = \begin{pmatrix} q_{11}^{(i)} & q_{12}^{(i)} \\ q_{21}^{(i)} & q_{22}^{(i)} \end{pmatrix} \begin{pmatrix} A_i \\ C_i \end{pmatrix}. \tag{1}$$

The entries of the scattering matrix in Eq. (1) can be analytically computed using parameters related to the electromagnetic analysis and the geometry. Let (t_{1i}, t_{2i}) and (k_{1i}, k_{2i}) be defined

as the *through-coupled* and *cross-coupled* field coefficients at the ring-waveguide coupling areas (grey areas in Fig. 2), respectively. Let η_i^2 be the *ring round-trip transmission factor*, which can be numerically computed from the mode analysis. The coefficient η_i depends on the phase constant and the field attenuation after half of the microring as

$$\eta_i = \exp[-\pi r_i(\alpha_i^r - j\beta_i^r)] \tag{2}$$

where r_i is the microring radius, β_i^r is the phase constant and α_i^r is the field attenuation of the ith microring. As a result, the entries of the scattering matrix are

$$q_{11}^{(i)} = \frac{t_{1i} - \eta_i^2 t_{2i}^*(|t_{1i}|^2 + |\kappa_{1i}|^2)}{1 - \eta_i^2 t_{1i}^* t_{2i}^*}, \tag{3a}$$

$$q_{12}^{(i)} = -\frac{\kappa_{1i}\kappa_{2i}^*\eta_i}{1 - \eta_i^2 t_{1i}^* t_{2i}^*}, \tag{3b}$$

$$q_{21}^{(i)} = -\frac{\kappa_{1i}^*\kappa_{2i}\eta_i}{1 - \eta_i^2 t_{1i}^* t_{2i}^*}, \tag{3c}$$

$$q_{22}^{(i)} = \frac{t_{2i} - \eta_i^2 t_{1i}^*(|t_{2i}|^2 + |\kappa_{2i}|^2)}{1 - \eta_i^2 t_{1i}^* t_{2i}^*}, \tag{3d}$$

where the asterisk denotes the complex conjugate [27]. Since the through-coupled and cross-coupled field coefficients and the round trip transmission factor depend on the optical wavelength, the entries of the scattering matrix in Eq. (3) also depend on the wavelength.

Thanks to the large coupling coefficients, a negligible backscattering can be assumed [28].

The output field D_i of block i is related to the input field C_{i+1} by the following phase shift relation

$$C_{i+1} = \tau_i D_i. \tag{4}$$

The constant τ_i has the same form of Eq. (2) and it depends on the distance between two rings L_i as

$$\tau_i = \exp[-L_i(\alpha^w - j\beta^w)], \tag{5}$$

where β^w and α^w are the phase constant and the field attenuation of the waveguide, respectively.

The input/output relation can be derived by combining the previous formulas

$$\begin{pmatrix} B_i \\ C_{i+1} \end{pmatrix} = \begin{pmatrix} 1 & 0 \\ 0 & \tau_i \end{pmatrix} \begin{pmatrix} B_i \\ D_i \end{pmatrix} = \begin{pmatrix} 1 & 0 \\ 0 & \tau_i \end{pmatrix} \boldsymbol{Q}^{(i)} \begin{pmatrix} A_i \\ C_i \end{pmatrix}. \tag{6}$$

For a compact notation, let us introduce the matrix $\boldsymbol{P}^{(i)}$

$$\begin{pmatrix} B_i \\ C_{i+1} \end{pmatrix} = \boldsymbol{P}^{(i)} \begin{pmatrix} A_i \\ C_i \end{pmatrix} = \begin{pmatrix} q_{11}^{(i)} & q_{12}^{(i)} \\ \tau_i q_{21}^{(i)} & \tau_i q_{22}^{(i)} \end{pmatrix} \begin{pmatrix} A_i \\ C_i \end{pmatrix}. \tag{7}$$

A. Bus NoC Scattering Matrix

To compute the input/output transfer matrix of bus NoC in Fig. 1(a) for $n = 4$, the scattering matrices are combined, leading to

$$\begin{pmatrix} O_0 \\ O_1 \\ O_2 \\ O_3 \\ O_4 \end{pmatrix} = \begin{pmatrix} 1-w & \boldsymbol{u}^T \\ \boldsymbol{v} & \boldsymbol{M} \end{pmatrix} \begin{pmatrix} I_0 \\ I_1 \\ I_2 \\ I_3 \\ I_4 \end{pmatrix}, \tag{8}$$

where w is a scalar, $\boldsymbol{u}^T$ is 1×4 row vector, $\boldsymbol{v}$ is 4×1 column vector, and $\boldsymbol{M}$ is a 4×4 square matrix

$$w = 1 - p_{22}^{(4)} p_{22}^{(3)} p_{22}^{(2)} p_{22}^{(1)},$$

$$\boldsymbol{u} = \begin{pmatrix} p_{22}^{(4)} p_{22}^{(3)} p_{22}^{(2)} p_{21}^{(1)} \\ p_{22}^{(4)} p_{22}^{(3)} p_{21}^{(2)} \\ p_{22}^{(4)} p_{21}^{(3)} \\ p_{21}^{(4)} \end{pmatrix}, \quad \boldsymbol{v} = \begin{pmatrix} p_{12}^{(1)} \\ p_{12}^{(2)} p_{22}^{(1)} \\ p_{12}^{(3)} p_{22}^{(2)} p_{22}^{(1)} \\ p_{12}^{(4)} p_{22}^{(3)} p_{22}^{(2)} p_{22}^{(1)} \end{pmatrix},$$

$$\boldsymbol{M} = \begin{pmatrix} p_{11}^{(1)} & 0 & 0 & 0 \\ p_{12}^{(2)} p_{21}^{(1)} & p_{11}^{(2)} & 0 & 0 \\ p_{12}^{(3)} p_{22}^{(2)} p_{21}^{(1)} & p_{12}^{(3)} p_{21}^{(2)} & p_{11}^{(3)} & 0 \\ p_{12}^{(4)} p_{22}^{(3)} p_{22}^{(2)} p_{21}^{(1)} & p_{12}^{(4)} p_{22}^{(3)} p_{21}^{(2)} & p_{12}^{(4)} p_{21}^{(3)} & p_{11}^{(4)} \end{pmatrix}. \tag{9}$$

Without loss of generality, we assumed that the length of the bus waveguide from the input port I_0 to the first microring is negligible (i.e., $L_0 = 0$), allowing an easier derivation of the coefficients in Eq. (9). Equations (8) and (9) can be easily generalized in the case of n blocks. Indeed, by introducing the vectors

$$\boldsymbol{O} = \begin{pmatrix} O_1 \\ \vdots \\ O_n \end{pmatrix}, \qquad \boldsymbol{I} = \begin{pmatrix} I_1 \\ \vdots \\ I_n \end{pmatrix}, \tag{10}$$

Eq. (8) becomes

$$\begin{pmatrix} O_0 \\ \boldsymbol{O} \end{pmatrix} = \begin{pmatrix} 1-w & \boldsymbol{u}^T \\ \boldsymbol{v} & \boldsymbol{M} \end{pmatrix} \begin{pmatrix} I_0 \\ \boldsymbol{I} \end{pmatrix} \tag{11}$$

where $\boldsymbol{M}$ is an $n \times n$ matrix, $\boldsymbol{u}$ and $\boldsymbol{v}$ are column vectors of n elements.

B. Ring NoC Scattering Matrix

The scattering matrix of the ring NoC can be derived from Eq. (11) with the constraint $I_0 = O_0$. This condition forces the signal to recirculate in the shared ring. From Eq. (11)

$$wI_0 = \boldsymbol{u}^T \boldsymbol{I}, \tag{12a}$$

$$\boldsymbol{O} = \boldsymbol{v} I_0 + \boldsymbol{M}\boldsymbol{I}, \tag{12b}$$

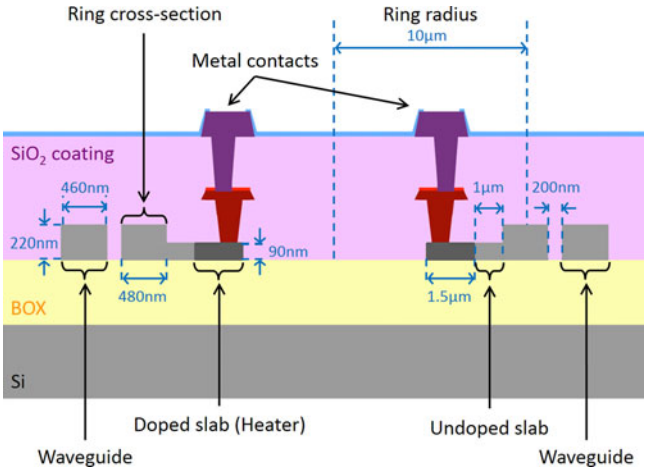

Fig. 3. Schematic of the microring cross-section.

and the input/output relation is

$$\boldsymbol{O} = \left[\frac{1}{w}\boldsymbol{v}\boldsymbol{u}^T + \boldsymbol{M}\right]\boldsymbol{I} = \boldsymbol{N}\,\boldsymbol{I}, \tag{13}$$

where $\boldsymbol{N}$ is an $n \times n$ matrix obtained by adding the matrix $\boldsymbol{v}\boldsymbol{u}^T/w$ (responsible for the recirculating signal) to the matrix $\boldsymbol{M}$.

IV. PIC Design

The considered bus and ring NoCs (see Fig. 1) have been designed and fabricated as a PIC. The PICs were fabricated through CMC Microsystems by the Institute of Microelectronics, Singapore, on 220-nm silicon-on-insulator wafers. The cross-section of one of the add/drop microrings and its input and output waveguides is schematically shown in Fig. 3. Each microring is made of silicon, with a cross-section of 480 nm $\times$ 220 nm and a radius of 10 μm. Each microring is fabricated on a 2 μm-thick buried silicon oxide layer and it is coated by a silica cladding. As shown in Fig. 3, a 90-nm-high slab is added only on the inner side of the microring. The external section of the slab (next to the microring) is kept undoped, while the internal section is doped with phosphorus at a peak doping concentration of 5×10^{20} cm^{-3} [29]. The resonance frequency of each microring is thermally tuned by injecting a current in the conductive path created by the doped slab. The presence of a slab only on the inner side of the ring allows the reduction of the bending loss and the improvement of the thermal isolation of the input/output waveguides. On the other hand, the undoped slab allows the enhancement of the heat transfer from the doped slab to the ring waveguide, since silicon is characterized by a thermal conductivity higher than that of silica (i.e., $k_{Si} = 149$ Wm^{-1}K^{-1} and $k_{SiO2} = 1.3$ Wm^{-1}K^{-1}). The thermal conductivity of n-doped silicon is assumed to be equal to 60 Wm^{-1}K^{-1} [30].

The two NoCs are designed for transmission at 10 Gb/s with ON–OFF keyed nonreturn-to-zero signals. For small microring loss ($4\pi r_i \alpha_i^r \ll |k_{1i}|^2 + |k_{2i}|^2$), the BW$_i$ of the add/drop microring is proportional to the square of the coupling coefficients (i.e., BW$_i \sim |k_{1i}|^2 + |k_{2i}|^2$). Not only are large coupling coefficients beneficial for the BW, but also for keeping XT limited

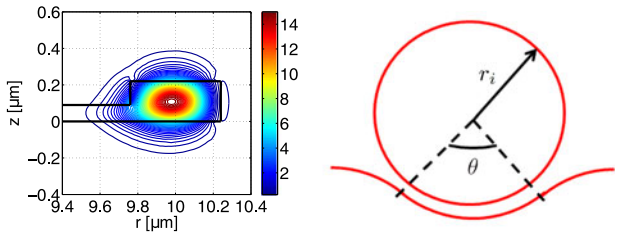

Fig. 4. Microring mode analysis and coupler design. (a) Normalized mode intensity profile measured in $1/\mu\text{m}^2$. (b) Bended coupled waveguide.

[20]. To prevent that fabrication inaccuracies reduce the BW below the requirement, in the PIC design phase the power coupling coefficients are set equal to 10% (i.e., $|k_{1i}|^2 = |k_{2i}|^2 = 0.1$ for $i = 1, \ldots, n$), which leads to a 3-dB transmission BW of around 28 GHz.

The presence of the slab on the inner side of the microring moves the electromagnetic mode closer to the internal wall of the microring, as shown in Fig. 4(a). In addition, since the minimum fabrication gap between rib waveguides is 200 nm (minimum exclusion rule), the highest coupling coefficient between the microring and the straight waveguide is around 2%–3%. Therefore, to achieve the required coupling coefficient, the input/output waveguides are narrowed (i.e., 460-nm-wide) and the length of the coupling region is lengthened by bending the coupled waveguide of an angle $\theta = 32°$, as shown in Fig. 4(b) [31].

In the ring NoC, the length of the shared ring l has been set so that the ratio between the free spectral range of each microring (FSR) and the shared ring (fsr) is four [20], i.e.,

$$\frac{\text{FSR}}{\text{fsr}} = \frac{l\, n_g^w}{2\pi r_i\, n_g^r} = 4, \tag{14}$$

where n_g^r and n_g^w are the group indices of the microring and the shared ring, respectively.

The pictures of the fabricated PICs are displayed in Fig. 5(a) and (b) for the bus and ring NoCs, respectively. For both architectures, single-polarization (transverse electric) grating couplers are used to interface the fibers to the PIC [32]. In the figures, T_i ($0 \le i \le 2$ in the bus and $1 \le i \le 4$ in the ring) indicate where the transmitters (with lasers and modulators) are to be connected. Similarly, R_i ($0 \le i \le 2$ in the bus and $1 \le i \le 4$ in the ring) indicate where the receivers are to be connected.

V. Scattering Coefficients: Numerical and Experimental Results

This section presents the numerical and experimental results for the fabricated NoCs. Here and in the following section the analysis of the NoC is focused on the worst case scenario from the perspective of XT, which is the most detrimental impairment for the performance of the two PICs.

When two optical transmissions interfere, two scenarios of XT are possible: if the corresponding carrier wavelengths are identical or very close, the XT is named *homo-wavelength XT*; vice versa, when the two signals propagate on different carriers, then the corresponding noise is called *hetero-wavelength*

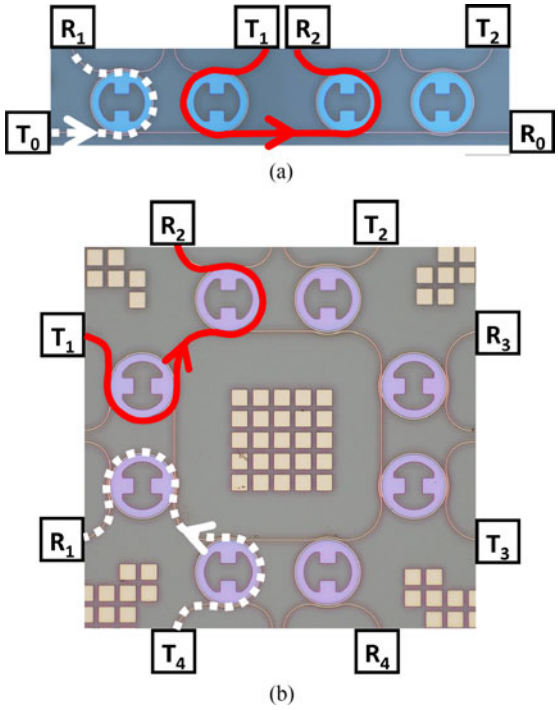

Fig. 5. Photonic integrated NoCs. (a) PIC of the bus NoC. (b) PIC of the ring NoC.

XT [19], [21]. While the hetero-wavelength XT can be reduced by filtering the signals (which is also performed by microrings at the receiver side [19], [23]), the homo-wavelength XT cannot be removed and for this reason it is the most deteriorating source of noise. In this scenario, a single-hop transmission induces the highest XT on downstream transmissions at the same wavelength. The XT is maximized when single-hop transmissions on the same wavelength are set between all adjacent ports [20]. In this context, the stronger interference is caused by the immediately downstream single-hop transmission, as mathematically shown in [20].

For the NoC designs in Fig. 5, the ports with transmitters T_i (receivers R_i) are the even (odd) ports in Eqs. (8) and (13), that is:

$$\begin{pmatrix} T_1 \\ T_2 \\ \vdots \\ T_{n/2} \end{pmatrix} = \begin{pmatrix} I_2 \\ I_4 \\ \vdots \\ I_n \end{pmatrix}, \qquad \begin{pmatrix} R_1 \\ R_2 \\ \vdots \\ R_{n/2} \end{pmatrix} = \begin{pmatrix} O_1 \\ O_3 \\ \vdots \\ O_{n-1} \end{pmatrix}, \tag{15}$$

where n is an even number.

For the bus NoC, transmitter T_0 is connected to the input port I_0 and receiver R_0 is connected to the output port O_0, i.e.,

$$T_0 = I_0, \qquad R_0 = O_0. \tag{16}$$

In the presence of homo-wavelength XT, using the notation introduced in Section III, the scattering matrices for the bus and ring NoCs shown in Fig. 5(a) and (b) become, respectively

$$\begin{pmatrix} R_0 \\ R_1 \\ R_2 \end{pmatrix} = \begin{pmatrix} 1-w & u_2 & u_4 \\ v_1 & 0 & 0 \\ v_3 & M_{32} & 0 \end{pmatrix} \begin{pmatrix} T_0 \\ T_1 \\ T_2 \end{pmatrix}, \tag{17}$$

$$\begin{pmatrix} R_1 \\ R_2 \\ R_3 \\ R_4 \end{pmatrix} = \begin{pmatrix} N_{12} & N_{14} & N_{16} & N_{18} \\ N_{32} & N_{34} & N_{36} & N_{38} \\ N_{52} & N_{54} & N_{56} & N_{58} \\ N_{72} & N_{74} & N_{76} & N_{78} \end{pmatrix} \begin{pmatrix} T_1 \\ T_2 \\ T_3 \\ T_4 \end{pmatrix}. \tag{18}$$

Since the network is reciprocal and since the coupling coefficients, microring distances, microring sizes and microring resonance wavelengths are the same for the various ports, some identities appear in the scattering coefficients.

For the bus NoC, the transfer function v_1 (i.e., communication $T_0 \rightarrow R_1$) has the same behaviour of u_4 (i.e., the communication link $T_2 \rightarrow R_0$). Similarly, v_3 and u_2 must be identical since the corresponding communication ($T_1 \rightarrow R_0$ and $T_0 \rightarrow R_2$) are specular. As a result, in Eq. (17), only four of six coefficients are independent. The scattering coefficient u_4 is the drop transfer function of a single-microring filter. The scattering coefficient M_{32} is the drop transfer function of two uncoupled microrings in cascade (the extinction ratio of M_{32} is twice of u_4). The scattering coefficient $(1-w)$ is the through transfer function of a four uncoupled microrings rings in cascade. The scattering coefficients u_2 is the product of the drop transfer function of a single microring and the through transfer function of two uncoupled microrings in cascade: it has the shape of a drop transfer function (such as u_4) combined with the "notch" shape of the through transfer function (such as $1-w$). The four independent scattering coefficients of the bus NoC are reported in Fig. 6 as a function of the wavelength.

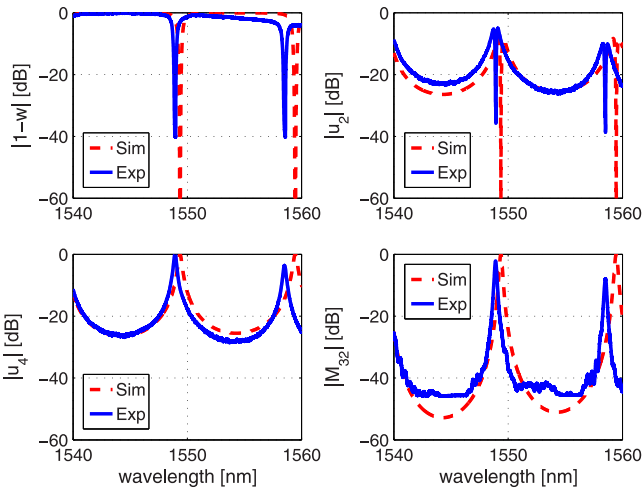

Fig. 6. Scattering coefficients of the bus NoC.

In the figure, the numerical (dashed curves) and the experimental results (solid curves) show a good agreement between

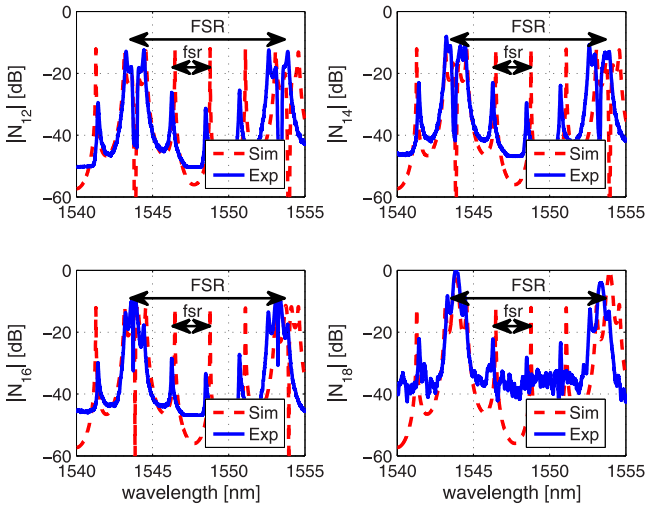

Fig. 7. Scattering coefficients of the ring NoC.

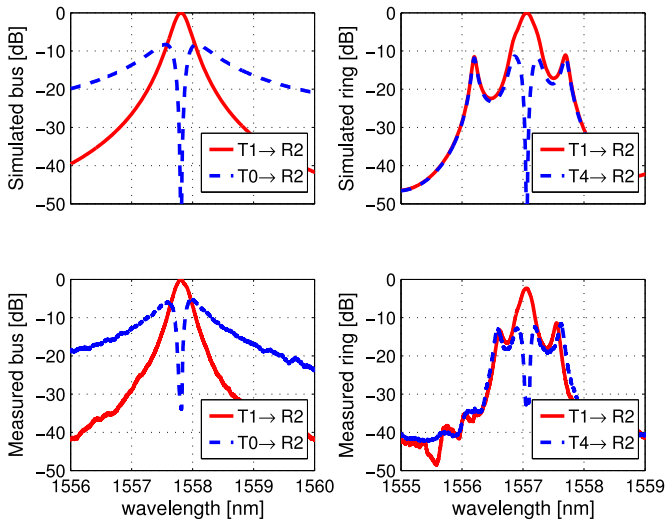

Fig. 8. Transfer functions at receiver R_2 simulated (top) and measured (bottom) for the bus (left) and ring (right) architectures, when transmitting from T_1 (solid lines) and when transmitting from the upstream transmitter to the upstream receiver (dashed lines representing the homo-wavelength XT) .

theory and measurements. The small mismatch of the FSR is due to the fabrication inaccuracies (e.g., roughness, doping inaccuracies) of the waveguides. Moreover, in the experimental curves the peaks at higher wavelengths have smaller amplitude and the envelope of $|1 - w|$ is not flat. This is caused by the transfer function of the Bragg-grating used to couple the light in and out of the PIC [32].

Similarly, for the ring NoC only four of the sixteen scattering coefficients are independent. Indeed, the transfer function between a transmitter and the four receivers is the same as when the transmitter is shifted by one position. As a result, the matrix in Eq. (18) becomes a circulant matrix with elements

$$N_{12} = N_{34} = N_{56} = N_{78}, \tag{19a}$$

$$N_{14} = N_{36} = N_{58} = N_{72}, \tag{19b}$$

$$N_{16} = N_{38} = N_{52} = N_{74}, \tag{19c}$$

$$N_{18} = N_{32} = N_{54} = N_{76}. \tag{19d}$$

Similar results are shown in Fig. 7 for the ring NoC. For symmetry reasons, only the coefficients of the first row of matrix $\boldsymbol{N}$ are reported. Also in this case, simulated and measured scattering coefficients exhibit a good agreement between theory and experiments. In all the subplots of Fig. 7, two FSRs can be identified: the band between the sharp peaks is about 2.4 nm and it is due to the fsr of shared ring, while the periodicity of the scattering coefficients is about 9.62 nm and it is related to FSR of the add/drop microrings [20].

The homo-wavelength XT is now assessed for the single one-hop transmission $T_1 \rightarrow R_2$ (indicated with a solid line in Fig. 5(a) and (b)). This communication can be affected by a homo-wavelength XT due to another one-hop upstream transmission at the same wavelength: $T_0 \rightarrow R_1$ and $T_4 \rightarrow R_1$ transmissions in the bus and ring NoC, respectively (indicated with a dashed line in Fig. 5(a) and (b)). Thus, receiver R_2 receives the intended transmission ($T_1 \rightarrow R_2$) as well as the signal that is not dropped by the upstream receiver R_1, leading to XT.

TABLE I
SIMULATIONS AND MEASUREMENTS COMPARISON

	Bus		Ring	
	sim.	meas.	sim.	meas.
BW	28.6 GHz	27.8 GHz	28.7 GHz	22.2 GHz
XT	−16.9 dB	−11.2 dB	−017.9 dB	−17.9 dB

Notice that in the bus NoC, injecting the signal from the bus (T_0) instead of an upstream transmitter is a worst case scenario for the interference.

A magnification of the scattering coefficients at receiver R_2 is reported in Fig. 8, where the simulated (top) and measured (bottom) transfer functions are compared for the bus (left) and the ring (right) NoCs. In all the subplots, solid curves refer to the intended transmission $T_1 \rightarrow R_2$. The transfer functions of the upstream signal at R_2 are also shown with dashed curves and represent the XT on $T_1 \rightarrow R_2$. In the ring NoC, the interference spectra outside the 10-dB BW is much lower than in the bus architecture and has secondary peaks. This difference is caused by the filtering behaviour and the resonance of the shared ring. In the figure, the simulation results and the measurements of the NoCs are in good matching.

The comparison of the measured and simulated BW and XT are reported in Table I for the bus and the ring architectures, respectively. The small differences between theory and experiments are mainly due to the fabrication inaccuracies of the ring-waveguide gap and, as a consequence, of the power coupling coefficients and therefore the BW. On the other hand, the microring resonance alignment procedure is mainly responsible for the small differences on the XT level.

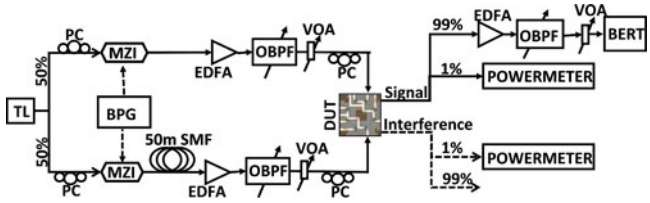

Fig. 9. Experimental setup.

VI. BER Performance Evaluation

The transmission performance of both NoCs under investigation has been evaluated in terms of BER measurements.

Two different transmission configurations are compared for both the ring and bus architectures: (i) one single one-hop transmission ($T_1 \rightarrow R_2$) and (ii) two simultaneous transmissions in which another one-hop upstream transmission ($T_4 \rightarrow R_1$ in the ring architecture; $T_0 \rightarrow R_1$ in the bus architecture) can cause interference to the transmission $T_1 \rightarrow R_2$. For both the architectures, the BER has been measured for the transmission between the port T_1 and the port R_2.

Fig. 9 shows the experimental setup for the BER performance evaluation. A tunable laser emits at 1550 nm an optical power of 10 dBm. The linewidth is set to 100 MHz by activating the coherence control. This signal is divided into two arms by a 3 dB optical splitter. In each arm, the signal is modulated by a Mach–Zehnder Interferometer fed by a $2^{31}-1$ pseudo random binary sequence at 10 Gb/s produced by the bit pattern generator. The signals are de-correlated by a 50 m single mode fiber spool inserted in one arm before being amplified by two different erbium doped fiber amplifiers (EDFA), filtered by two 1-nm-wide optical band pass filters (OBPF) and then power controlled using two variable optical attenuators (VOA). Two 8-port fiber arrays are used to inject/extract light to/from the device under test (DUT) by two 8-port TE grating coupler arrays with a pitch of 127 μm. The optical coupling into the DUT is optimized by two polarization controllers. A multiprobe is used to contact an array of ten pads with a pitch of 200 μm for independently tuning the microrings. At the receiver side, the output signal at the port R_2 of the DUT is amplified by an EDFA and filtered by a 1.2-nm-wide OBPF. The optical power at the photodetector is controlled by a VOA, while the optical signal-to-noise ratio is kept constant at 38 dB.

Fig. 10 shows the BER versus the optical power received at port R_2 including the back-to-back (B2B) measurements as reference. For a single transmission, the ring architecture achieves a BER lower than the bus architecture and mildly outperforms B2B. Both these results are due to the filtering effect of the microrings that act as adapted receivers leading to an increase of the sensitivity, as also described first in [12].

In the presence of the interference due to the adjacent upstream transmission, the BER values of both architectures are comparable, and no impact of the recirculation of residual signal in the shared ring is observed. On the other hand, the interference caused by the non-adjacent upstream transmissions is negligible (e.g., $T_3 \rightarrow R_4$ in the ring NoC), as theoretically and experimentally demonstrated for the ring NoC in [20] and [23], respectively.

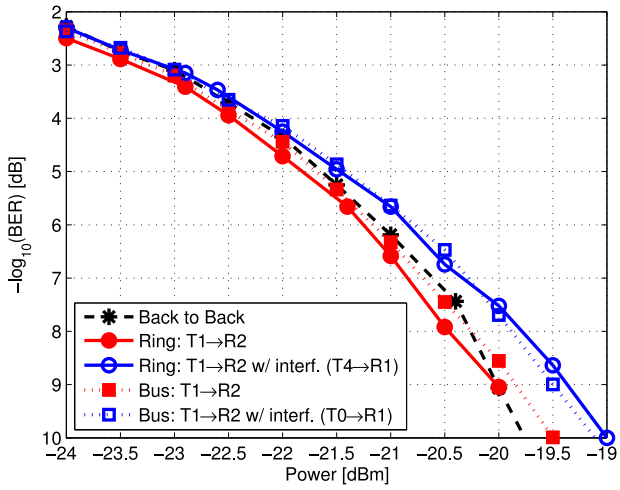

Fig. 10. BER measurements at receiver R_2 for transmission $T_1 \rightarrow R_2$ in the presence and absence of a simultaneous upstream transmission.

VII. Conclusion

This paper presented a theoretical framework based on transfer matrices suitable for the design and analysis of different microring-based NoC topologies. More specifically, the paper compared the theoretical and experimental performance of two NoCs with bus and ring topologies, realized with silicon-based PIC. The presented theoretical framework is able to well predict the spectral performance of the PICs. The BER measurements indicate that NoC can well support one or multiple transmissions at 10 Gb/s on the same wavelength. In particular, the BER of the ring NoC outperforms the back-to-back measurements, thanks to the filtering effects of the microrings. In the bus NoC, the filtering effects are limited by the different topology (i.e., no central shared ring), leading to small penalty of about 0.5 dB for a BER of 10^{-9}.

Acknowledgment

The authors would like to thank NSERC SiEPIC Program for the training and the component library, and CMC Microsystems for the foundry service and fruitful technical discussions. A special thanks to Dr. G. Contestabile of Scuola Superiore Sant'Anna for insightful discussion and advice.

References

[1] J. Kim, K. Choi, and G. Loh, "Exploiting new interconnect technologies in on-chip communication," *IEEE J. Emerging Sel. Topics Circuits Syst.*, vol. 2, no. 2, pp. 124–136, Jun. 2012.

[2] A. Shacham, K. Bergman, and L. Carloni, "Photonic networks-on-chip for future generations of chip multiprocessors," *IEEE Trans. Comput.*, vol. 57, no. 9, pp. 1246–1260, Sep. 2008.

[3] Y. Pan, P. Kumar, J. Kim, G. Memik, Y. Zhang, and A. Choudhary, "Firefly: Illuminating future network-on-chip with nanophotonics," in *Proc. Annu. Int. Symp. Comput. Archit.*, 2009, pp. 429–440.

[4] G. Chen, H. Chen, M. Haurylau, N. A. Nelson, D. H. Albonesi, P. M. Fauchet, and E. G. Friedman, "Predictions of CMOS compatible on-chip optical interconnect," *Integration, VLSI J.*, vol. 40, no. 4, pp. 434–446, 2007.

[5] A. Benner, "Cost-effective optics: Enabling the exascale roadmap," in *Proc. IEEE 17th Symp. High Performance Interconnects*, Aug. 2009, pp. 133–137.

[6] D. Ding and D. Z. Pan, "Oil: A nano-photonics optical interconnect library for a new photonic networks-on-chip architecture," in *Proc. Int. Workshop Syst. Level Interconnect Prediction*, 2009, pp. 11–18.
[7] C. Arellano, S. Mingaleev, E. Sokolov, and A. Richter, "The power of circuit simulations for designing photonic integrated circuits," *Concurrency Comput., Practice Exp.*, vol. 26, no. 15, pp. 2518–2529, 2014.
[8] N. Kirman, M. Kirman, R. K. Dokania, J. F. Martinez, A. B. Apsel, M. A. Watkins, and D. H. Albonesi, "Leveraging optical technology in future bus-based chip multiprocessors," in *Proc. IEEE/ACM Int. Symp. Microarchit.*, 2006, pp. 492–503.
[9] G. Kurian, J. E. Miller, J. Psota, J. Eastep, J. Liu, J. Michel, L. C. Kimerling, and A. Agarwal, "ATAC: A 1000-core cache-coherent processor with on-chip optical network," in *Proc. 19th Int. Conf. Parallel Archit. Compilation Tech.*, 2010, pp. 477–488.
[10] S. L. Beux, J. Trajkovic, I. O'Connor, and G. Nicolescu, "Layout guidelines for 3d architectures including optical ring network-on-chip (ORNOC)," in *Proc. IEEE/IFIP 19th Int. Conf. VLSI Syst. Chip*, 2011, pp. 242–247.
[11] A. Biberman, H. Lira, K. Padmaraju, N. Ophir, J. Chan, M. Lipson, and K. Bergman, "Broadband silicon photonic electrooptic switch for photonic interconnection networks," *IEEE Photon. Technol. Lett.*, vol. 23, no. 8, pp. 504–506, Apr. 2011.
[12] A. Parini, G. Bellanca, A. Annoni, F. Morichetti, A. Melloni, M. Strain, M. Sorel, M. Gay, C. Pareige, and L. Bramerie, "BER evaluation of a passive SOI WDM router," *IEEE Photon. Technol. Lett.*, vol. 25, no. 23, pp. 2285–2288, Dec. 2013.
[13] L. Chen and Y. Chen, "Compact, low-loss and low-power 8×8 broadband silicon optical switch," *Opt. Exp.*, vol. 20, pp. 18977–18985, 2012.
[14] A. Joshi, C. Batten, Y.-J. Kwon, S. Beamer, I. Shamim, K. Asanovic, and V. Stojanovic, "Silicon-photonic CLOS networks for global on-chip communication," in *Proc. ACM/IEEE 3rd Int. Symp. Netw.-Chip*, 2009, pp. 124–133.
[15] D. Vantrease, R. Schreiber, M. Monchiero, M. McLaren, N. P. Jouppi, M. Fiorentino, A. Davis, N. Binkert, R. G. Beausoleil, and J. H. Ahn, "Corona: System implications of emerging nanophotonic technology," *ACM SIGARCH Comput. Archit. News*, vol. 36, no. 3, pp. 153–164, 2008.
[16] Y. Pan, P. Kumar, J. Kim, G. Memik, Y. Zhang, and A. Choudhary, "Firefly: Illuminating future network-on-chip with nanophotonics," *ACM SIGARCH Comput. Archit. News*, vol. 37, no. 3, pp. 429–440, 2009.
[17] X. Zhang and A. Louri, "A multilayer nanophotonic interconnection network for on-chip many-core communications," in *Proc. Des. Autom. Conf.*, 2010, pp. 156–161.
[18] Y. Pan, J. Kim, and G. Memik, "Flexishare: Channel sharing for an energy-efficient nanophotonic crossbar," in *Proc. Int. Symp. High Performance Comput. Archit.*, 2010, pp. 1–12.
[19] J. Zhou, M. O'Mahony, and S. Walker, "Analysis of optical crosstalk effects in multi-wavelength switched networks," *IEEE Photon. Technol. Lett.*, vol. 6, no. 2, pp. 302–305, Feb. 1994.
[20] P. Pintus, P. Contu, P. Raponi, I. Cerutti, and N. Andriolli, "Silicon-based all-optical multi microring network-on-chip," *Opt. Lett.*, vol. 39, pp. 797–800, 2014.
[21] P. Pintus, P. Contu, N. Andriolli, A. D'Errico, F. Di Pasquale, and F. Testa, "Analysis and design of microring-based switching elements in a silicon photonic integrated transponder aggregator," *J. Lightw. Technol.*, vol. 31, no. 24, pp. 3943–3955, Dec. 2013.
[22] F. Gambini, P. Pintus, S. Faralli, N. Andriolli, and I. Cerutti, "A photonic integrated network-on-chip with multi microrings," presented at the Optical Fiber Communications Conf., Los Angeles, CA, USA, 2015.
[23] F. Gambini, S. Faralli, P. Pintus, N. Andriolli, and I. Cerutti, "BER evaluation of a low-crosstalk silicon integrated multi-microring network-on-chip," *Opt. Exp.*, vol. 23, no. 13, pp. 17169–17178, Jun. 2015.
[24] S. Faralli, F. Gambini, P. Pintus, I. Cerutti, and N. Andriolli, "Ring versus bus: A BER comparison of photonic integrated networks-on-chip," presented at the Optical Interconnects Conf., San Diego, CA, USA, 2015.
[25] I. Cerutti, N. Andriolli, P. Pintus, S. Faralli, F. Gambini, P. Castoldi, and O. Liboiron-Ladouceur, "Fast scheduling based on iterative parallel wavelength matching for a multi-wavelength ring network-on-chip," presented at the Optical Network Design Modeling, Pisa, Italy, 2015, p. We8.3O.
[26] M. Watts, W. Zortman, D. Trotter, G. Nielson, D. Luck, and R. Young, "Adiabatic resonant microrings (ARMs) with directly integrated thermal microphotonics," presented at the Conf. Lasers Electro-Optics, Baltimore, MD, USA, 2009.
[27] J. Capmany, P. Muñoz, J. Domenech, and M. Muriel, "Apodized coupled resonator waveguides," *Opt. Exp.*, vol. 15, pp. 10196–10206, 2007.
[28] F. Morichetti, A. Canciamilla, M. Martinelli, A. Samarelli, R. De La Rue, M. Sorel, and A. Melloni, "Coherent backscattering in optical microring resonators," *Appl. Phys. Lett.*, vol. 96, no. 8, p. 081112, 2010.
[29] M. Streshinsky, A. Ayazi, Z. Xuan, A. E.-J. Lim, G.-Q. Lo, T. Baehr-Jones, and M. Hochberg, "Highly linear silicon traveling wave Mach-Zehnder carrier depletion modulator based on differential drive," *Opt. Exp.*, vol. 21, pp. 3818–3825, 2013.
[30] L. Wenjun, K. Etessam-Yazdani, R. Hussin, and M. Asheghi, "Modeling and data for thermal conductivity of ultrathin single-crystal SOI layers at high temperature," *IEEE Trans. Electron Devices*, vol. 53, no. 8, pp. 1868–1876, Aug. 2006.
[31] D. Spencer, J. Bauters, M. Heck, and J. Bowers, "Integrated waveguide coupled Si3N4 resonators in the ultrahigh-Q regime," *Optica*, vol. 1, pp. 153–157, 2014.
[32] Y. Wang, J. Flueckiger, C. Lin, and L. Chrostowski, "Universal grating coupler design," *Proc. SPIE, Photon. North*, vol. 8915, pp. 89150Y-1–89150Y-7, 2013.

Authors' biographies not available at the time of publication.